Brain Multiphysics 4 (2023) 100071

Contents lists available at ScienceDirect

Brain Multiphysics

journal homepage: www.sciencedirect.com/journal/brain-multiphysics

Multi-physics modeling and finite-element formulation of neuronal dendrite growth with electrical polarization

Shuolun Wang [a,*], Xincheng Wang [a], Maria A. Holland [a,b]

[a] Department of Aerospace and Mechanical Engineering, University of Notre Dame, Notre Dame, IN 46556, USA
[b] Bioengineering Graduate Program, University of Notre Dame, Notre Dame, IN 46556, USA

ARTICLE INFO

Dataset link: https://github.com/mholla/BMPHI23

Keywords:
Neuronal dendrites
Turing patterns
Finite element modeling
Convolutional neural network

ABSTRACT

The neuron serves as the basic computational unit for the brain. Altered neuronal morphologies are usually found in various neurological diseases, such as Down syndrome, Williams syndrome, and idiopathic autism. Compelling biological evidence demonstrates that neuronal morphology can be dynamically regulated by neuronal activity through the mediation of calcium signaling pathways. Moreover, studies have revealed that exposure to an applied electric field can induce directional migration of neurites toward the cathode. In this study, we developed a coupled system that combines an advective Gray–Scott model with Gauss's law to gain a better understanding of dendrite growth and response to electrical polarization. Our simulation results successfully capture key features such as dendrite branching, space-filling, self-avoidance, and electrical polarization. With the help of the convolutional neural network, we inversely identified model parameters of real dendrite morphologies from an online open source. Finally, we calibrated our model using experimental data on growing neurons under applied electric fields.

1. Introduction

The nervous system comprises a vast number of neurons with different morphologies [1]. A typically-developed neuron roughly consists of a soma or cell body, multiple dendrites, a single axon, and synapses [2]. Neuronal dendrites are tree-like protrusions from the soma and receive incoming electrical signals from other neurons' synapses. The axon also protrudes from the soma and can extend as far as one meter in humans under stretch growth [3]. At the other end of the axon are synapses, where the fired electrical signal goes across and passes down to the subsequent neurons.

Dendrites are a unique neural component, distinguished by their intricate morphologies, which enable them to perform vital functions. Their signature branching feature allows multiple connections between neurons, thus facilitating high connectivity in the brain [4]. Another critical feature of dendrite morphology is "tiling" – nonredundant innervation of a receptive area by the same type of neurons – which serves as a universal organizing principle across species. With the help of the photo-filling technique, MacNeil and Masland (1998) [5] discovered that similar visual neurons in rabbits form their territories and barely overlap. This arrangement makes functional sense because it allows the incoming light to fall onto as many different types of visual neurons as possible [6]. In *Drosophila*, the dendrites of class III and IV neurons also exhibit the "tiling" phenomenon, occupying their individual spaces while preventing overlap at the borders [7,8]. Extensive studies in computational neuroscience have been aimed at unraveling the relationship between dendrite morphology and their transmission of electrical signals [9–11]. However, the question of how dendrite morphology is formed during neural development needs to be better understood.

While various mechanisms can impact dendritic development, neuronal activity plays a crucial role in shaping dendritic morphology through the process of calcium signaling [12]. Calcium ions (Ca^{2+}) are essential for neuronal signaling (Fig. 1), and they enter neurons through various channels, including ligand-gated channels (LGCs), N-methyl-D-aspartate receptors (NMDARs), and voltage-gated calcium channels (VGCCs). When Ca^{2+} enters, it binds to calmodulin, which in turn binds to the calcium/calmodulin-dependent protein kinases (CaMKs), leading to their activation and phosphorylation. Studies have shown that activated CaMKII exerts a positive impact on the extension of filopodia and the growth of fine dendrites through its direct interaction with cytoskeletal actin, in contrast to other CaMKs that have differing effects on dendrites [13–15].

Dendrite growth could also be influenced by many extrinsic factors. It has been found that brain-derived neurotrophic factor (BDNF), Neurotrophin 3, and nerve growth factor (NGF) could either promote or inhibit dendrite outgrowth in vertebrates [16]. Numerous molecules

* Corresponding author.
E-mail address: swang25@nd.edu (S. Wang).

https://doi.org/10.1016/j.brain.2023.100071
Received 20 January 2023; Received in revised form 25 April 2023; Accepted 26 April 2023
Available online 2 May 2023

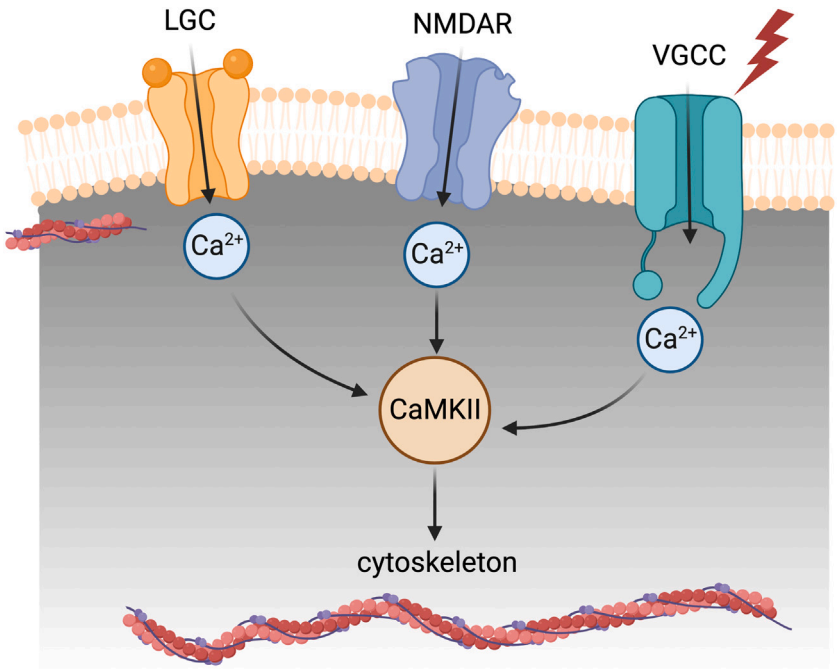

Fig. 1. Schematics of the biological process that might regulate dendritic growth. When calcium Ca^{2+} enters the neuron through different channels, it activates calcium/calmodulin-dependent protein kinase II (CaMKII), phosphorylating the cytoskeleton. LGC, ligand-gated channels; NMDAR, N-methyl-D-aspartate receptor; VGCC, voltage-gated calcium channels.

have been discovered for their roles in pathfinding and guidance, such as the chemoattractant Semaphorin 3 A, whose spatial gradient may pattern the growth of apical dendrites towards the pial surface [17,18]. The endogenous electric field also changes in space and time throughout embryonic development, guiding neuronal migration [19]. Early work showed that neurites in embryonic chicks grow faster towards the cathode than the anode in an applied electric field [20]. More sophisticated experiments have provided evidence of electric field-induced polarization in human neural stem cells as well [21]. Nevertheless, the electric field does not stand alone in neural polarization; the work by McCaig et al. (2000) [22] hinted that neurotrophins and endogenous electric fields are likely to interact *in vivo* during nervous system development.

There are many diverse mathematical models of neural development [23–25]. Early works attempted to generate artificial dendrites by following statistical distributions of geometrical properties gathered from experiments [26,27]. More recently, agent-based models have provided more realistic results by using measured tip growth dynamics as input data [8]. Models that minimize wiring capture dendrite morphology reasonably well, but need more plausible explanations for the underlying cellular processes [28,29]. Continuum models that incorporate the idea of the like-repel-like mechanism resemble a Turing system (diffusion–reaction of two morphogens), which could capture the space-filling and "tiling" in *Drosophila* [30,31]. Recently, a phase-field model based on isogeometric collocation captured the neural growth process, including initial neurite outgrowth, axon differentiation, and dendrite formation [32]. Axon guidance is influenced by chemoattractants, chemorepellents, and contact signals [33,34], and various models have been developed to capture these interactions, including finite-dimensional state vector models, probabilistic models, and hybrid models that combine a random walk method with the diffusion of chemical species [35–37]. A few studies have incorporated mechanics into the framework, studying the viscoelastic deformation of the axonal shaft [38] and durotaxis [39] – cell migration guided by stiffness gradients – to understand how axons navigate their environment.

The objective of this research is to gain insights into the intricate biological processes that underlie dendritic growth through employing a multi-physics model and numerical simulations. Our model builds upon the diffusion–reaction framework proposed by Sugimura et al. (2007) [30] but the biological relevance is enhanced by new evidence highlighting the impact of CaMKII activation via Ca^{2+} signaling on dendrite growth. Our model formulation differs from previous diffusion–reaction models by adopting a precursor–product relationship between Ca^{2+} and activated CaMKII, as opposed to the conventional activator–inhibitor relationship. We incorporated electrical polarization as a simple advection term in our system. Meanwhile, our model is implemented numerically using the finite-element method, which enables us to accurately solve for patterns in arbitrary geometries, as opposed to using the finite difference method [30]. Finally, we set up a convolutional neural network to relate our model to reality, which inversely identifies model parameters from real neuron images.

2. Methods

This section introduces our proposed multi-physics model that captures dendrite growth under the influence of the applied electric field. We also discuss the details of our finite-element implementations and convolutional neural network setup for inverse neural pattern recognitions.

2.1. Mathematical modeling

Evolution of neuronal dendrites: Dendritic growth may be modulated by calcium signaling. As reported in the biological literature [12–14], calcium ions enter neurons through multiple channels and then bind with calmodulin, leading to the activation of CaMKII. Ultimately, activated CaMKII phosphorylates the cytoskeleton, a crucial constituent of the dendrite (Fig. 1).

Our model considers Ca^{2+} and activated CaMKII as two morphogens, denoted as U and V, respectively, which can diffuse and mutually influence each other. In contrast to the conventional activator–inhibitor relationship between two morphogens [30], we propose a hypothetical precursor–product association between Ca^{2+} and activated

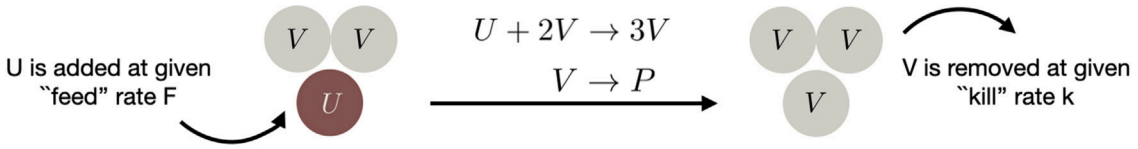

Fig. 2. Schematic of the Gray–Scott model. Two molecules of morphogen V react with one molecule of morphogen U to form three molecules of morphogen V. Morphogen U is fed into the reaction at a given "feed" rate F, while morphogen V is removed and turned into product P at a given "kill" rate k.

CaMKII, which forms the basis of the Gray–Scott model [40,41] in our study. The model has the following reaction,

$$\begin{aligned} U + 2V &\longrightarrow 3V, \\ V &\longrightarrow P \end{aligned} \tag{2.1}$$

in the domain $\mathcal{B}$ (Fig. 2). The first reaction requires one unit of U to react with two units of V to produce three units of V. The second reaction turns one unit of V into one unit of product P. By continuously adding U with a "feed" rate F and removing product P and excessive V with a "kill" rate k, the system will drift away from the equilibrium, producing intricate patterns as nonlinear dynamics unfolds [42].

Calcium signaling can also explain the behavior of dendrites under an electric field. When an electric field is applied, dendrites tend to move toward the cathode. This is due to the entry of calcium ions through depolarized VGCCs, which activate more CaMKII [19–22,43,44]. In order to effectively represent the electrical polarization in our model, we have introduced an advection term exclusively to the morphogen V, representing CaMKII, which more directly contributes to the formation of the dendrite structure than Ca^{2+}. This modification has resulted in an advective Gray–Scott model,

$$\begin{cases} \dot{u} = D_u \nabla^2 u \underbrace{-uv^2 + F(1-u)}_{g(u,v)}, \\ \dot{v} + \sigma \mathbf{E} \cdot \nabla v = D_v \nabla^2 v \underbrace{+uv^2 - (F+k)v}_{h(u,v)}, \end{cases} \tag{2.2}$$

where u and v are spatial densities of the diffusive and reactive morphogens; D_u and D_v are the corresponding diffusion coefficients; $g(u,v)$ and $h(u,v)$ are reaction terms; F and k are the feeding rate of u and the draining rate of v, respectively; and $\mathbf{E}$ is the electric field with parameter σ controlling the polarization strength. The stability analysis of the above system without advection is elaborated in Appendix A.

Next, we introduce a phase variable c to represent the dendritic region primarily composed of the cytoskeleton. Because cytoskeletal components diffuse only limited distances in dendrites [45], it is possible to solve this moving boundary problem using an ordinary differential equation rather than a phase-field partial differential equation. From Sugimura et al. (2007) [30], we adopt a piecewise ODE to describe the transition between the bistable states of the absence or presence of the dendrite,

$$\dot{c} = \gamma c(a(v) - c)(c-1) \quad \text{with} \quad a(v) = \begin{cases} 0.49 & \text{when} \quad v \le T_r, \\ 0.49 - 2.5(v - T_r) & \text{when} \quad v > T_r, \end{cases} \tag{2.3}$$

where γ is a rate constant, $a(v) < 1$ is decreasing function of morphogen v, and T_r is a threshold value for morphogen v. Dendritic growth occurs only when $a(v) < 0$. It is worth noting that the phase variable c has two stable states, namely 0 and 1, corresponding to the absence and presence of the dendritic region, respectively.

Gauss's law: Neglecting electrodynamics effects, Gauss's law in the domain $\mathcal{B}$ is given by

$$\nabla \cdot \mathbf{D} = q, \tag{2.4}$$

where the vector field $\mathbf{D} = \epsilon \mathbf{E}$ is the electric displacement with ϵ denoting the permittivity. By the standard definition, the electric field is given by the negative of the gradient of the electric potential, $\mathbf{E} = -\nabla \Phi$. The quantity q on the RHS of Eq. (2.4) is the free charge density per unit volume. We simplify the brain tissue as an electrically insulating dielectric material, i.e., $q = 0$.

2.2. Initial boundary value problem and finite-element implementation

Here we briefly summarize the coupled partial differential equations and their strong forms given by

$$\left.\begin{aligned} \dot{u} &= D_u \nabla^2 u - uv^2 + F(1-u) \quad \text{in} \quad \mathcal{B}, \\ \dot{v} + \sigma \mathbf{E} \cdot \nabla v &= D_v \nabla^2 v + uv^2 - (F+k)v \quad \text{in} \quad \mathcal{B}, \end{aligned}\right\} \text{Transport of morphogens}$$

$$\left.\begin{aligned} \nabla^2 \Phi &= 0 \quad \text{in} \quad \mathcal{B}, \\ \Phi &= \check{\Phi} \quad \text{on} \quad \mathcal{S}_\Phi, \end{aligned}\right\} \text{Gauss's law} \tag{2.5}$$

where $\mathcal{S}_\Phi$ is the portion of the boundary with the prescribed electric potential $\check{\Phi}$.

Next, we let w_1, w_2, and w_3 denote three test fields that vanish on domain boundary $\mathcal{S}$. After multiplying the PDEs with three test fields and performing integration by parts, the weak form can be expressed as

$$\begin{cases} \displaystyle\int_{\mathcal{B}} w_1 \dot{u} dv + \int_{\mathcal{B}} \nabla w_1 \cdot D_u \nabla u dv + \int_{\mathcal{B}} w_1 uv^2 dv - \int_{\mathcal{B}} w_1 F(1-u) dv = 0, \\ \displaystyle\int_{\mathcal{B}} w_2 \dot{v} dv - \int_{\mathcal{B}} w_2 \sigma \nabla \Phi \cdot \nabla v dv + \int_{\mathcal{B}} \nabla w_2 \cdot D_v \nabla v dv \\ \quad \displaystyle - \int_{\mathcal{B}} w_2 uv^2 dv + \int_{\mathcal{B}} w_2 (F+k) v dv = 0, \\ \displaystyle\int_{\mathcal{B}} \nabla w_3 \cdot \nabla \Phi dv = 0. \end{cases} \tag{2.6}$$

As is routine, the body is discretized into finite elements such that $\mathcal{B} = \cup \mathcal{B}^e$, and the nodal variables are taken to be concentrations of morphogen u, v, and electric potential Φ, which are interpolated inside each element by

$$u = \sum u^A N^A, \qquad v = \sum v^A N^A, \qquad \text{and} \quad \Phi = \sum \Phi^A N^A \tag{2.7}$$

with the index $A = 1, 2, \ldots$ denoting the nodes of the element; N^A the shape functions; and u^A, v^A, and Φ^A representing the nodal concentrations of morphogens u and v and the electric potential Φ, respectively. Next, the test fields w_1, w_2, and w_3 are interpolated by the same shape functions in the Galerkin approach,

$$w_1 = \sum w_1^A N^A, \qquad w_2 = \sum w_2^A N^A, \qquad \text{and} \quad w_3 = \sum w_3^A N^A. \tag{2.8}$$

After substitution of Eq. (2.7) and Eq. (2.8) into the weak forms in Eq. (2.6), we arrive at element-level residuals of morphogen $u(\mathbf{x}, t)$, morphogen $v(\mathbf{x}, t)$, and electric field $\Phi(\mathbf{x}, t)$,

$$\begin{aligned} R_u^A = &\int_{\mathcal{B}^e} N^A \dot{u} dv + \int_{\mathcal{B}^e} \nabla N^A \cdot D_u \nabla u dv + \int_{\mathcal{B}^e} N^A uv^2 dv \\ &- \int_{\mathcal{B}^e} N^A F(1-u) dv, \end{aligned} \tag{2.9}$$

$$\begin{aligned} R_v^A = &\int_{\mathcal{B}^e} N^A \dot{v} dv - \int_{\mathcal{B}^e} N^A \sigma \nabla \Phi \cdot \nabla v dv + \int_{\mathcal{B}^e} \nabla N^A \cdot D_v \nabla v dv \\ &- \int_{\mathcal{B}^e} N^A uv^2 dv + \int_{\mathcal{B}^e} N^A (F+k) v dv, \quad \text{and} \end{aligned} \tag{2.10}$$

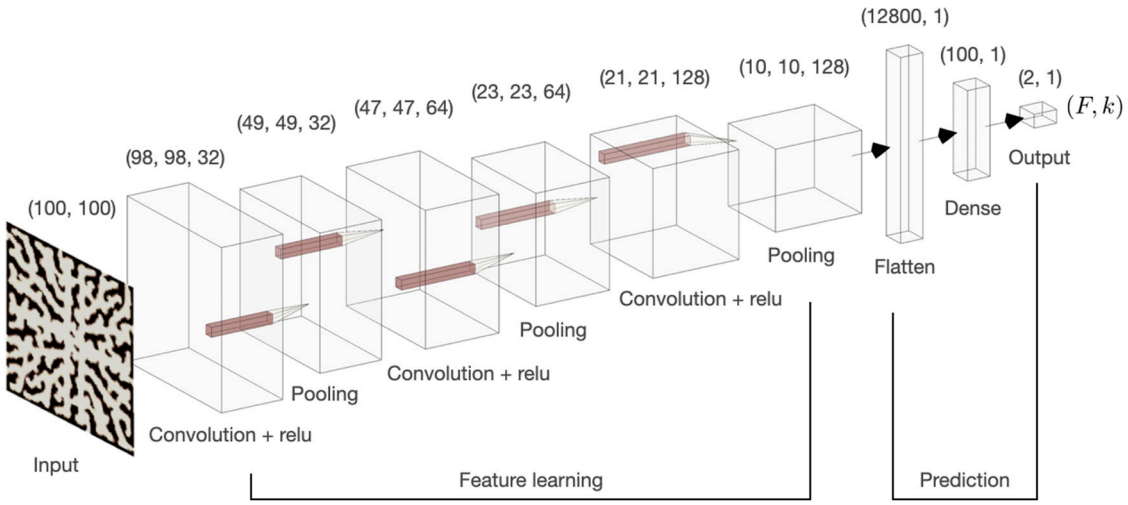

Fig. 3. Proposed CNN architecture for dendrites pattern recognitions. The input shown here is simulated phase variable c obtained from a 2-D simulation with 100 × 100 elements. The labels above each layer are corresponding data dimension settings in Tensorflow [46].

$$R^A_{\Phi} = \int_{\mathcal{B}^e} \nabla N^A \cdot \nabla \Phi \, dv. \tag{2.11}$$

These three element-level residuals are assembled into a global residual, which, when set to zero, represents a system of nonlinear equations for the nodal degrees of freedom.

The following tangents

$$(K_{uu})^{AB} = -\frac{\partial R^A_u}{\partial u^B}, \quad (K_{uv})^{AB} = -\frac{\partial R^A_u}{\partial v^B}, \quad (K_{u\Phi})^{AB} = -\frac{\partial R^A_u}{\partial \Phi^B}$$

$$(K_{vu})^{AB} = -\frac{\partial R^A_v}{\partial u^B}, \quad (K_{vv})^{AB} = -\frac{\partial R^A_v}{\partial v^B}, \quad (K_{v\Phi})^{AB} = -\frac{\partial R^A_v}{\partial \Phi^B},$$

$$(K_{\Phi u})^{AB} = -\frac{\partial R^A_{\Phi}}{\partial u^B}, \quad (K_{\Phi v})^{AB} = -\frac{\partial R^A_{\Phi}}{\partial v^B}, \quad (K_{\Phi\Phi})^{AB} = -\frac{\partial R^A_{\Phi}}{\partial \Phi^B},$$

are required by the iterative Newton–Raphson procedure for convergence. More specifically, the diagonal tangents are given by

$$K^{AB}_{uu} = -\int_{\mathcal{B}^e} N^A N^B \Delta t^{-1} dv - \int_{\mathcal{B}^e} \nabla N^A \cdot D_u \nabla N^B dv - \int_{\mathcal{B}^e} (F + v^2) N^A N^B dv, \tag{2.12}$$

$$K^{AB}_{vv} = -\int_{\mathcal{B}^e} N^A N^B \Delta t^{-1} dv + \int_{\mathcal{B}^e} N^A \sigma \nabla \Phi \cdot \nabla N^B dv - \int_{\mathcal{B}^e} \nabla N^A \cdot D_v \nabla N^B dv + \int_{\mathcal{B}^e} 2uv N^A N^B dv - \int_{\mathcal{B}^e} (F + k) N^A N^B dv, \quad \text{and} \tag{2.13}$$

$$K^{AB}_{\Phi\Phi} = -\int_{\mathcal{B}^e} \nabla N^A \cdot \nabla N^B dv, \tag{2.14}$$

and the off-diagonal tangents are given by

$$K^{AB}_{uv} = -\int_{\mathcal{B}^e} 2uv N^A N^B dv, \quad K^{AB}_{vu} = \int_{\mathcal{B}^e} v^2 N^A N^B dv, \quad \text{and} \quad K^{AB}_{v\Phi} = \int_{\mathcal{B}^e} N^A \sigma \nabla N^B \cdot \nabla v \, dv. \tag{2.15}$$

Note the electric field $\mathbf{E}$ is not coupled with morphogen u and only "one-way" coupled with the morphogen v; thus, we set off-diagonal tangents $K^{AB}_{u\Phi}$, $K^{AB}_{\Phi u}$, and $K^{AB}_{\Phi v}$ equal to zero.

The time integrations in Eqs. (2.2) and (2.3) are computed via the backward Euler method,

$$u_{n+1} = u_n + \Delta t \dot{u}_{n+1}, \quad v_{n+1} = v_n + \Delta t \dot{v}_{n+1}, \quad \text{and} \quad c_{n+1} = c_n + \Delta t \dot{c}_{n+1}, \tag{2.16}$$

where n and $n+1$ are the previous (known) and current (unknown) time steps, respectively.

We have implemented two-noded linear, four-noded quadrilateral (UPE4), and eight-noded brick (U3D8) elements, the first in Matlab and the latter two in Abaqus/Standard [47] by writing user-defined element (UEL) subroutines, following our previous work [48–52]. For a detailed verification procedure for our numerical implementation, readers could refer to Appendix B.

Table 1
Summary of material parameters.

Parameter [units]	Value	Source
Diffusivity D_v [$\mu m^2\ s^{-1}$]	0.1	[54]
Diffusivity ratio D_u/D_v [–]	[1–6]	[54]
Feeding rate F [s^{-1}]	[0–0.3]	[42]
Killing rate k [s^{-1}]	[0–0.08]	[42]
Polarization strength σ [$\mu m^2\ mV^{-1}\ s^{-1}$]	0.25	
Threshold value Tr [–]	0.1	[30]
Rate constant γ [s^{-1}]	10	[30]

2.3. Inverse pattern recognition via convolutional neural network

To inversely obtain parameters of F and k from real dendrite images, we utilized a convolutional neural network (CNN) – a machine learning method that is widely used for image recognition, speech translation, etc. [53] – as a surrogate model, and trained it with our finite-element simulations. Our CNN consists of feature-learning and prediction portions (Fig. 3). The feature-learning portion is a hierarchical structure built by repeatable convolutional layers with ReLU activation functions and max pooling layers. In contrast, the prediction portion is a fully connected neural network that collects information from the previous feature-learning portion. The detailed data structure settings used in each layer are shown in Fig. 3.

For our CNN training, the inputs are binary data of phase variable c obtained at each finite element. Correspondingly, the labeled outputs are rate constant pairs (F, k) used in the simulations. We have set up our CNN structure and training pipeline in Tensorflow [46].

3. Results and discussion

We simulate dendrite growth with electrical polarization using our proposed multi-physics model. We also demonstrate our model calibration to real neuron images via a CNN. Our intent here is to capture the phenomenon of dendrite growth via our modeling and simulation capabilities. Table 1 summarizes the model parameters used in the following simulations.

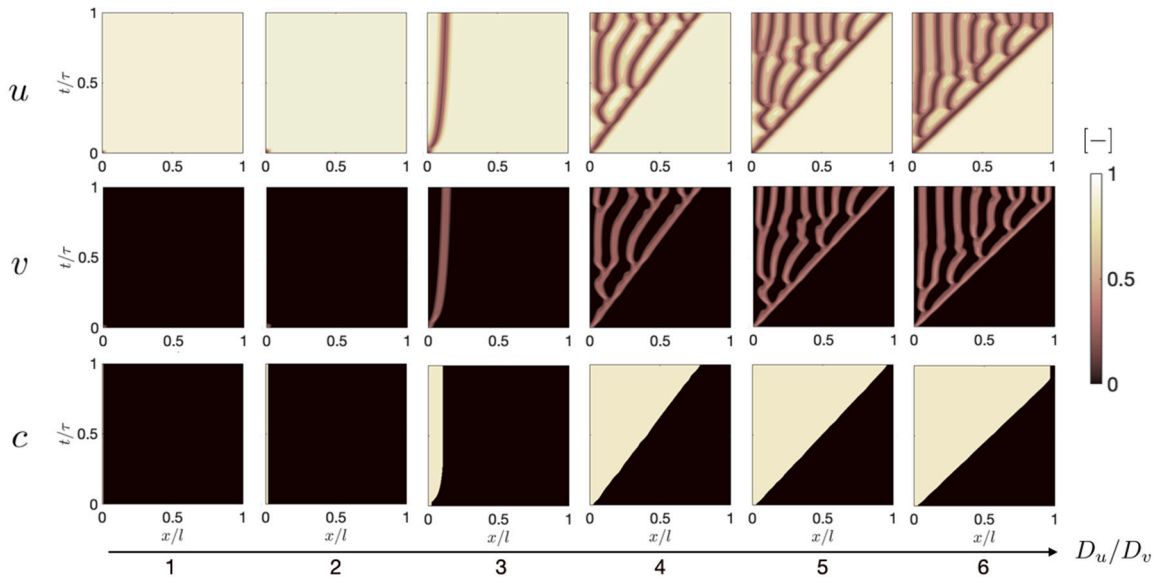

Fig. 4. The impact of diffusivity ratio D_u/D_v on spatial–temporal evolution of morphogens u and v, and phase variable c in 1-D problem.

3.1. Neuronal dendrite growth without polarization

Parametric study: Here we study the impact of various material parameters, including diffusivity ratio D_u/D_v and rate constant pair (F,k) on dendrite growth in the absence of applied electric fields. We start with a 1-D dendrite growth simulation that lasts for time τ. The computational domain with a length of l was discretized into 300 two-noded linear elements in Matlab. Initially, the soma covers a region of $0 \le x \le (4/300)l$, inside which we assigned $(u,v) = (0.5, 0.25)$, with $(u,v) = (1,0)$ assigned to the rest of the domain. Note that a non-zero initial phase variable $c_0 = 10^{-5}$ was chosen to make Eq. (2.3) numerically solvable. Additionally, we imposed zero flux boundary conditions at both ends of the domain to restrict any mass transfer across these boundaries.

For the parametric study, we first varied the diffusivity ratio D_u/D_v while keeping the rate constant pair fixed at $(F,k) = (0.028, 0.06)$ (Fig. 4). We observe that wave-splitting occurs at a diffusivity ratio around $D_u/D_v = 3$, which agrees with other results in the literature [55,56]. Additionally, both the speed and the number of wave-splitting (or branching) events increase with an increasing diffusivity ratio.

Next, we study the impact of rate constant pair (F,k) on dendrite growth at a fixed diffusivity ratio of $D_u/D_v = 4$, which is in line with the biological evidence that Ca^{2+} diffuse faster than CaMKII [54]. As expected, the whole domain is overwhelmed by morphogen u when either F or k dominates (Fig. 5), because either the calcium ion saturates or there is not enough CaMKII to consume it via reaction. When the rate constant pair (F,k) falls into an appropriate range, however, wave-splitting patterns with different "spacings" emerge.

As we extend the same analysis to 2-D cases with a fixed diffusivity ratio of $D_u/D_v = 3$, the system tends to exhibit an array of more vibrant patterns (Fig. 6, left). To explore all possible patterns compactly, we set the rate constant pair (F,k) as a function of 2-D space,

$$k(x) = k_{\min} + (k_{\max} - k_{\min})x/l \quad \text{and} \quad F(y) = F_{\min} + (F_{\max} - F_{\min})y/l, \tag{3.1}$$

where $k_{\min} = 0$, $k_{\max} = 0.08$, $F_{\min} = 0$, and $F_{\max} = 0.3$ are parameters used to bound $k \in [0, 0.08]$ and $F \in [0, 0.3]$ inside a square domain with a length of l. The simulated contour of u confirms that our stabilized boundary aligns with the bifurcation curve $F = 4(F+k)^2$, with intricate patterns emerging around the point $(F,k) = (1/16, 1/16)$, which is in agreement with previous stability analyses [55,57].

Following the seminal work on the Gray–Scott model [42], we located six representative patterns in our zoom-in $F-k$ diagram (Fig. 6, right) and simulated their pattern evolutions over time (Fig. 7). As an initial condition, all six cases start with soma seeds placed at the center, inside which we assigned $(u,v) = (0.5, 0.25)$, with $(u,v) = (1,0)$ assigned to the rest of the domain (Fig. 7). Furthermore, to prevent any mass transport across the boundaries, zero flux conditions are applied to the edges of the domain for all cases (Fig. 7). The case of "Mitosis" mimics a "cell division" process, in which the morphogen u tends to form dots and phase variable c creates the branching features of the neuron dendrites at the final stage. In the "Soliton" case, the morphogen u forms a mixture of dots and stripes, while the phase variable c captures thicker branching of dendrites. For the rest of the cases, the morphogen u tends to form mostly solid curves, while the phase variable c displays branching features with only small variations in the branch thickness.

Space-filling and self-avoidance: Here we examine our model's ability to reproduce features of space-filling and self-avoidance observed in dendrites [8,31]. To begin with, we conducted simulations of dendrite growth on ideal geometries featuring multiple soma seeds while enforcing zero flux conditions at the boundary (Fig. 8). During growth, dendrite arms extend spherically from each soma seed, undergo branching, and form boundaries once nearby dendrites are present. Two neurons in an oval domain form a "flat" boundary in between, while the five neurons in a pentagon form a pentagonal "pizza" (Fig. 8).

Next, we simulated the growth of class IV neurons in *Drosophila* larva and compared it qualitatively to experimental data [8]. The neurons in a *Drosophila* larva at 120 h were imaged in a 2-D slice viewed from the dorsal side by tagging transmembrane protein CD4 with a green fluorescent protein (GFP) (Fig. 9, right). We reproduced the 2-D geometry in our simulation, with a zero flux boundary condition at the larva's boundary, and placed 20 initial soma seeds according to the experiments.

Over the course of 96 hours, the dendrites migrate isotopically and occupy the entire domain, as expected. More interestingly, at 120 h, each simulated neuron has formed a rectangular-shaped compartment centered at its initial soma seed, which is in good qualitative agreement with the experiments (Fig. 9, left). These findings suggest that the Gray–Scott model, while phenomenological, captures the plausible morphogen interactions that lead to the dendrite patterns in the *Drosophila* larva. Further experimental research is needed to fully understand the underlying mechanisms that drive this neuronal development process.

Morphology analysis of real neurons via convolutional neural network: As mentioned before, we used a machine learning method –

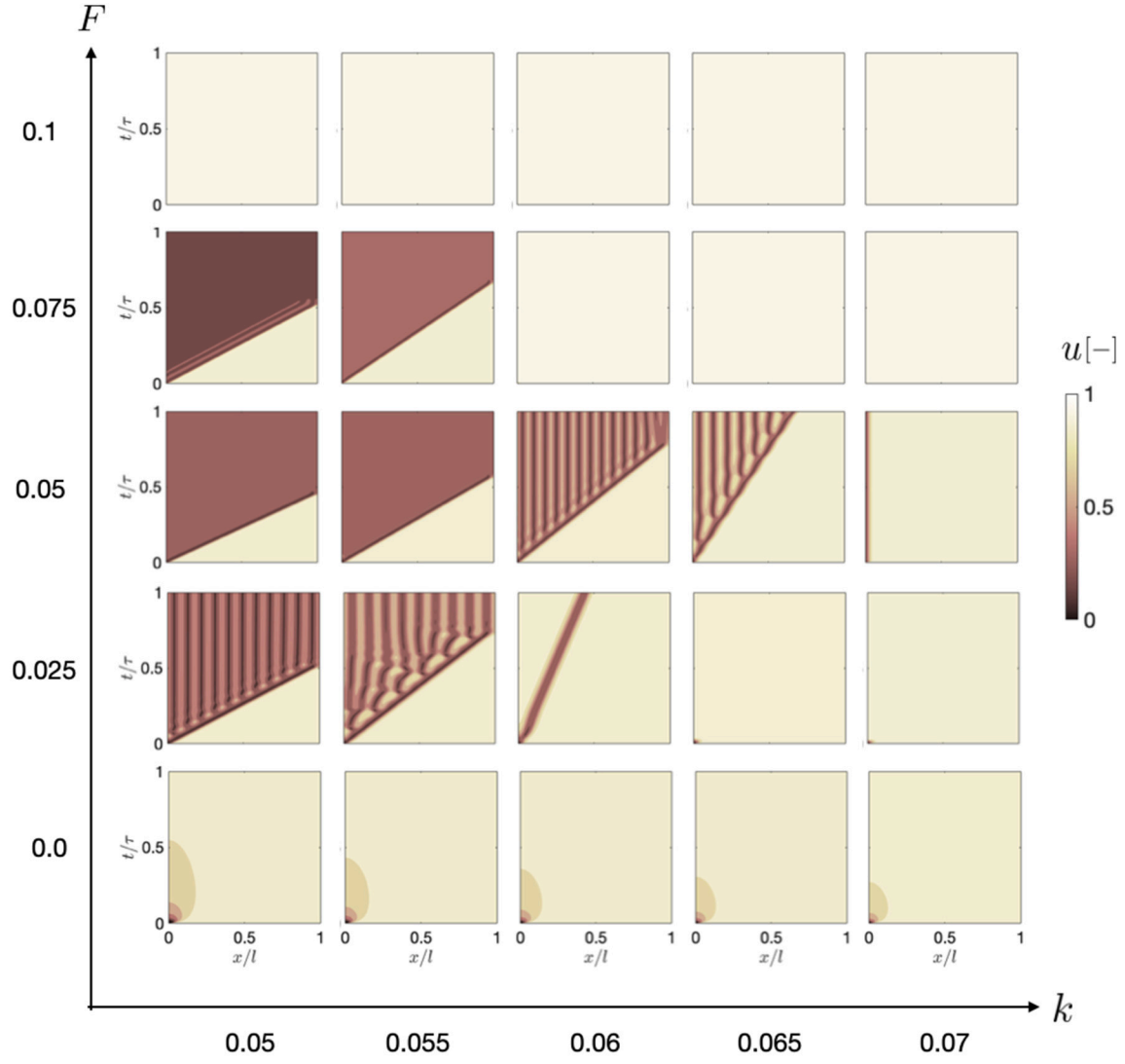

Fig. 5. The impact of rate constant pair (F, k) on spatial–temporal evolution of morphogen u in 1-D problem.

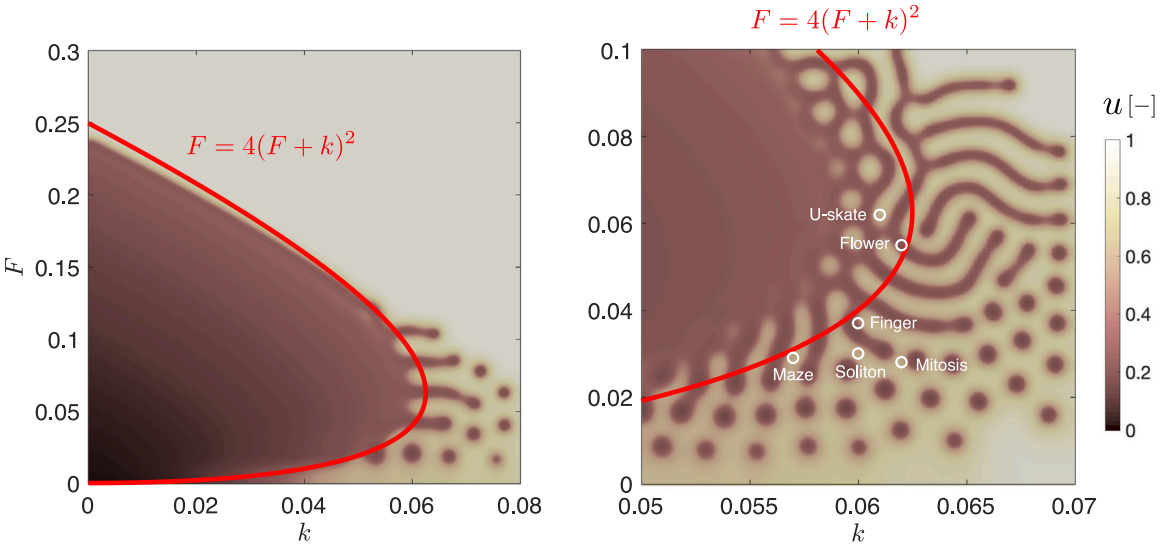

Fig. 6. The impact of rate constant pair (F, k) on spatial distribution of morphogen u at fixed diffusion ratio of $D_u/D_v = 3$ in the 2-D square domain with a length of l. Left: Full parameter coverage of $F \in [0, 0.3]$ and $k \in [0, 0.08]$. Right: A zoom-in parameter space of $F \in [0, 0.1]$ and $k \in [0.05, 0.07]$. Note we labeled six representative patterns in the zoom-in parameter space.

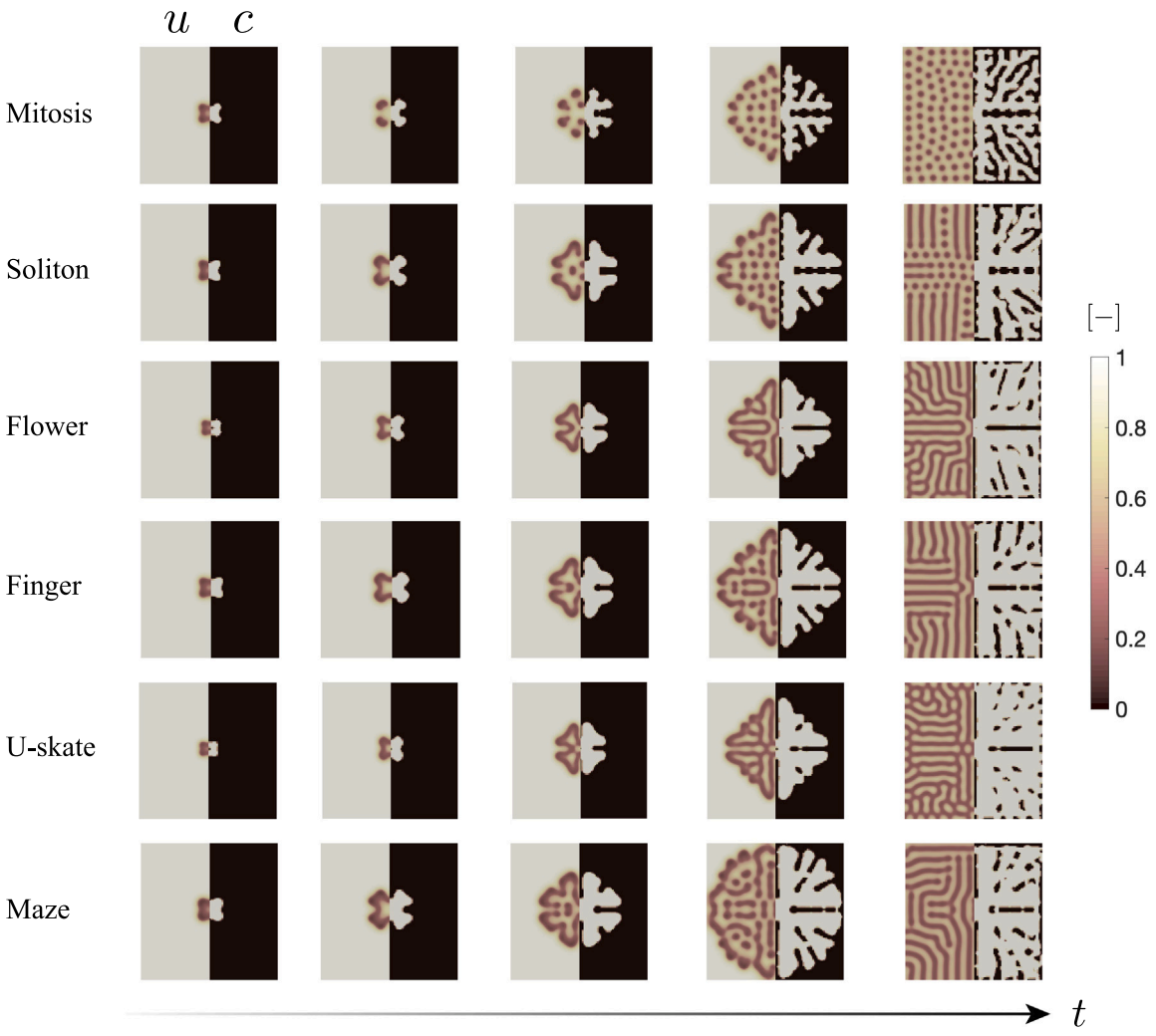

Fig. 7. The spatial–temporal evolution of morphogen u and phase variable c for six representative cases shown in Fig. 6, right.

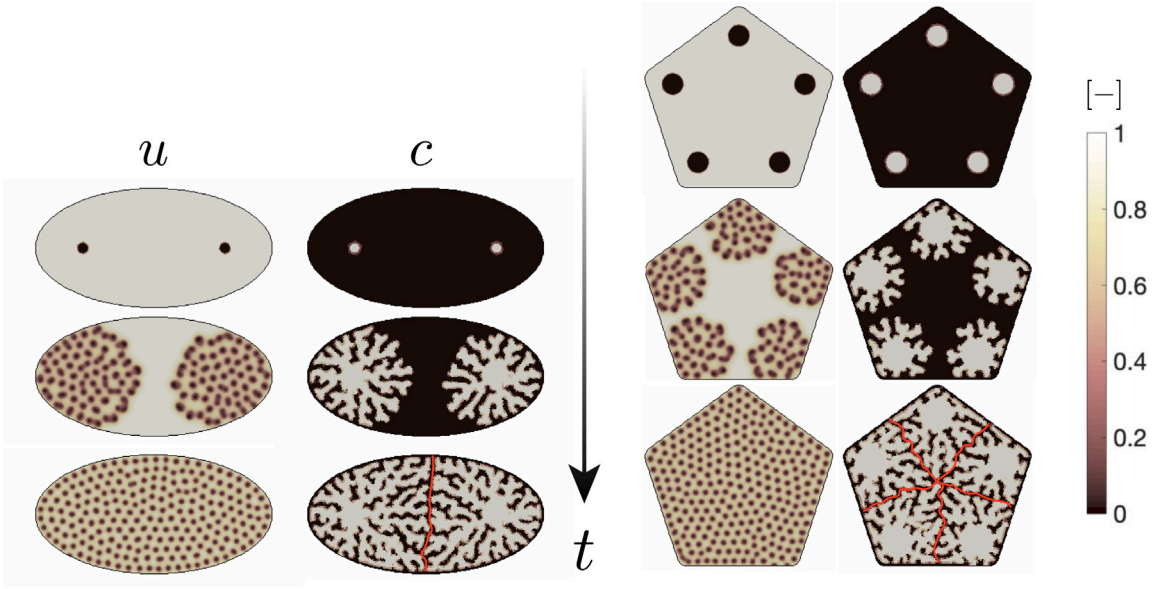

Fig. 8. The interactions between morphogen u and v accomplish features of space-filling and self-avoidance. The red lines denote inter-neuron boundaries in each contour plot of phase variable c. (For interpretation of the references to color in this figure legend, the reader is referred to the web version of this article.)

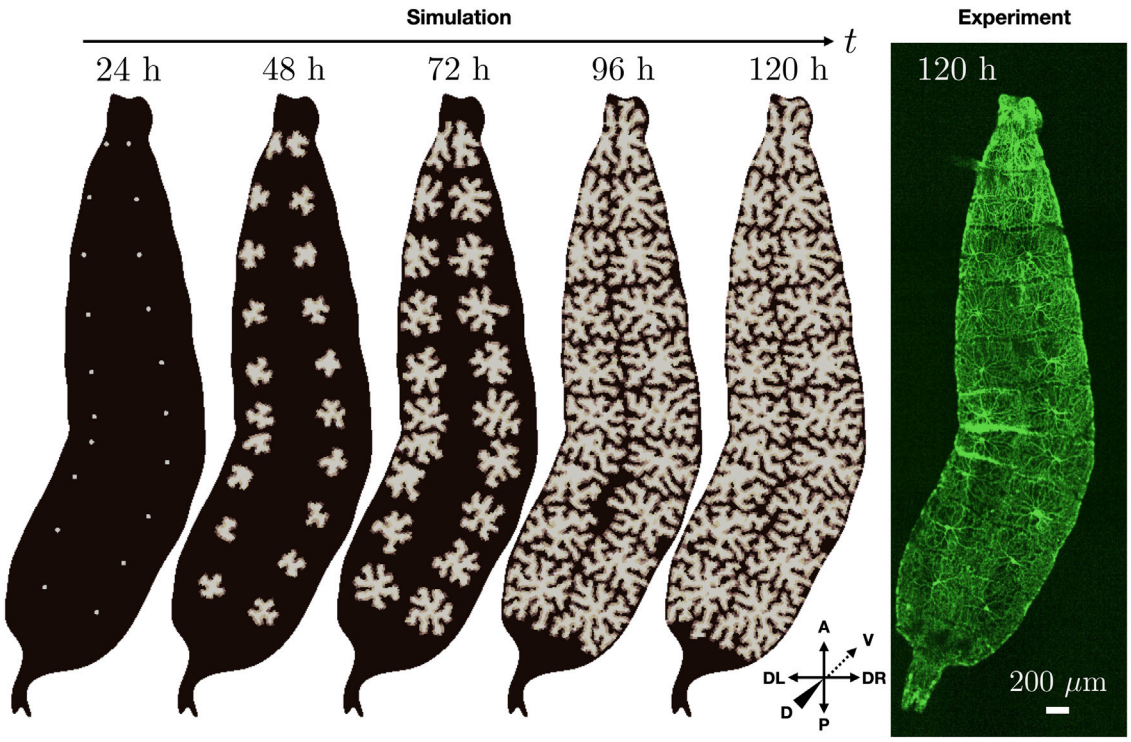

Fig. 9. Qualitative comparison between simulation and experiment [8] of class IV neurons in *Drosophila* larva during development (from 24 h to 120 h with egg lay defined as time zero). Neurons in the experiment are marked with the transmembrane protein CD4 tagged with a green fluorescent protein (GFP). The coordinates are added to show that the larva is viewed from the Dorsal (D) side, the Anterior (A) is up, the Posterior (P) is down, and the dashed arrow points in the Ventral (V) direction. Scale bar, 200 μm. (For interpretation of the references to color in this figure legend, the reader is referred to the web version of this article.)

convolutional neural network – to inversely obtain physical parameters from real dendrite morphologies.

For our initial training data pool, we prepared 100 2-D simulations with a fixed diffusivity ratio of $D_u/D_v = 3$, and covering a parameter space of $k \in [0.05, 0.07]$ and $F \in [0, 0.1]$ (Fig. 10a). Note that each simulation has 100×100 elements, and we used the elemental phase variable c at the final frame, when the system is in equilibrium, as training data. We then removed simulations that yield no patterns ($c = 0$ or 1 throughout the domain) since they are trivial and will confuse CNN with non-unique training labels. After data removal, the available training data pool was reduced to a dimension of $100^2 \times 40$. We then prepared a testing data pool with a dimension of $100^2 \times 16$, intentionally offsetting the training dataset in order to test the model's ability to extrapolate. We downloaded real images of dendrites in *Drosophila* larva, from which the CNN will eventually extract model parameters (Fig. 10b).

During training, the loss function (mean squared error) is minimized as the program iteratively optimizes the neural network weights [46]. The training history indicated that the loss function decays quickly after about the first 10 epochs (Fig. 11a). The neural network's performance on the testing dataset was recorded for later evaluation after each epoch, or a single iteration over the entire training dataset. We showed that the predicted rate constant pairs (F, k) are mostly sitting on top of the training ones (Fig. 11b). The CNN was also demonstrated to make reasonable extrapolations by yielding minor "displacements" between the testing and predicted dataset (Fig. 11c, green lines).

Finally, we used our fully-trained CNN to extract the rate constant pair (F, k) from five real neuron images. The results show that extracted parameters are all clustered at one spot in the $F - k$ diagram, which is to be expected because these five neurons were taken from a consistent region in *Drosophila* larva and thus share similar patterns (Fig. 11c). More importantly, our fully-trained CNN can provide consistent results even with noticeable differences like rotation angle and position among images (Fig. 10b).

3.2. Neuronal dendrite growth with electrical polarization

Homogeneous electric field: It has been reported that polarizations of dendrites could be guided by stimuli, such as chemo-attractant gradients, electric fields, and mechanical deformations [18,22,58]. Here we focus on simulating electric field-induced polarizations and calibrating our model to experiments by McCaig et al. (2000) [22].

In their experiment, neurons obtained from *Xenopus laevis* embryos were grown for $\tau = 5$ h in a uniform electric field with a magnitude of $|\mathbf{E}| = 150\,\mathrm{mV\,mm^{-1}}$. Neurons without any external stimulus served as controls. The experiments showed that the control samples grew relatively spherical, while stimulated neurons tended to grow towards the cathode (Fig. 12, upper panels). More importantly, the degree of polarization correlates positively with the strength of the electric field [22].

We captured the same observation in our simulation by turning polarization strength parameter σ on and off in Eq. (2.2) (Fig. 12, bottom panels). We also quantitatively compared our model against experiments in terms of the orientation distributions of dendrites (Fig. 13a, b). Our simple formulation allows us to vary polarization strength parameter σ, and we found that $\sigma\tau = 500\,\mu\mathrm{m^2\,mV^{-1}}$ yielded the lowest mean squared error (Fig. 13c) and captured the experiments reasonably well.

Inhomogeneous electric field: Here we run full 3-D simulations with inhomogeneous electrical polarizations. We demonstrate four different electrode setups in which the anode and cathode have potentials of $\Phi = \pm 75\,\mathrm{mV}$, respectively (Fig. 14). As expected, our electrode setups yield highly inhomogeneous electric potential distributions. The dendrites' growth aligns with the electric field $\mathbf{E}$ (red unit vectors) pointing toward the cathode.

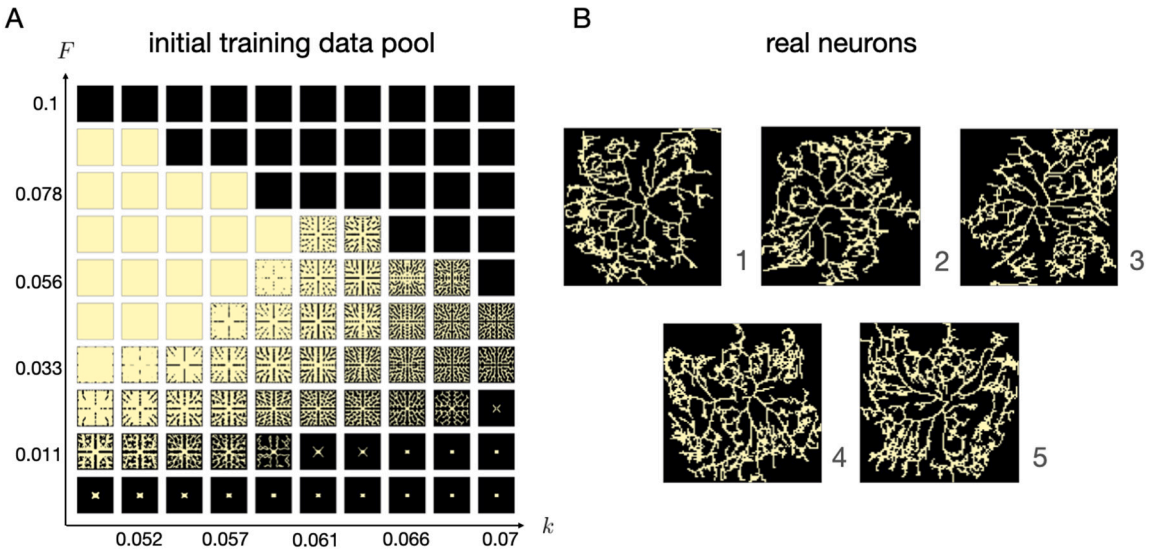

Fig. 10. Input data for CNN. (a) Initial training data pool, (b) real images of IV dendrites in *Drosophila* larva downloaded from an online open source [1]: https://neuromorpho.org/.

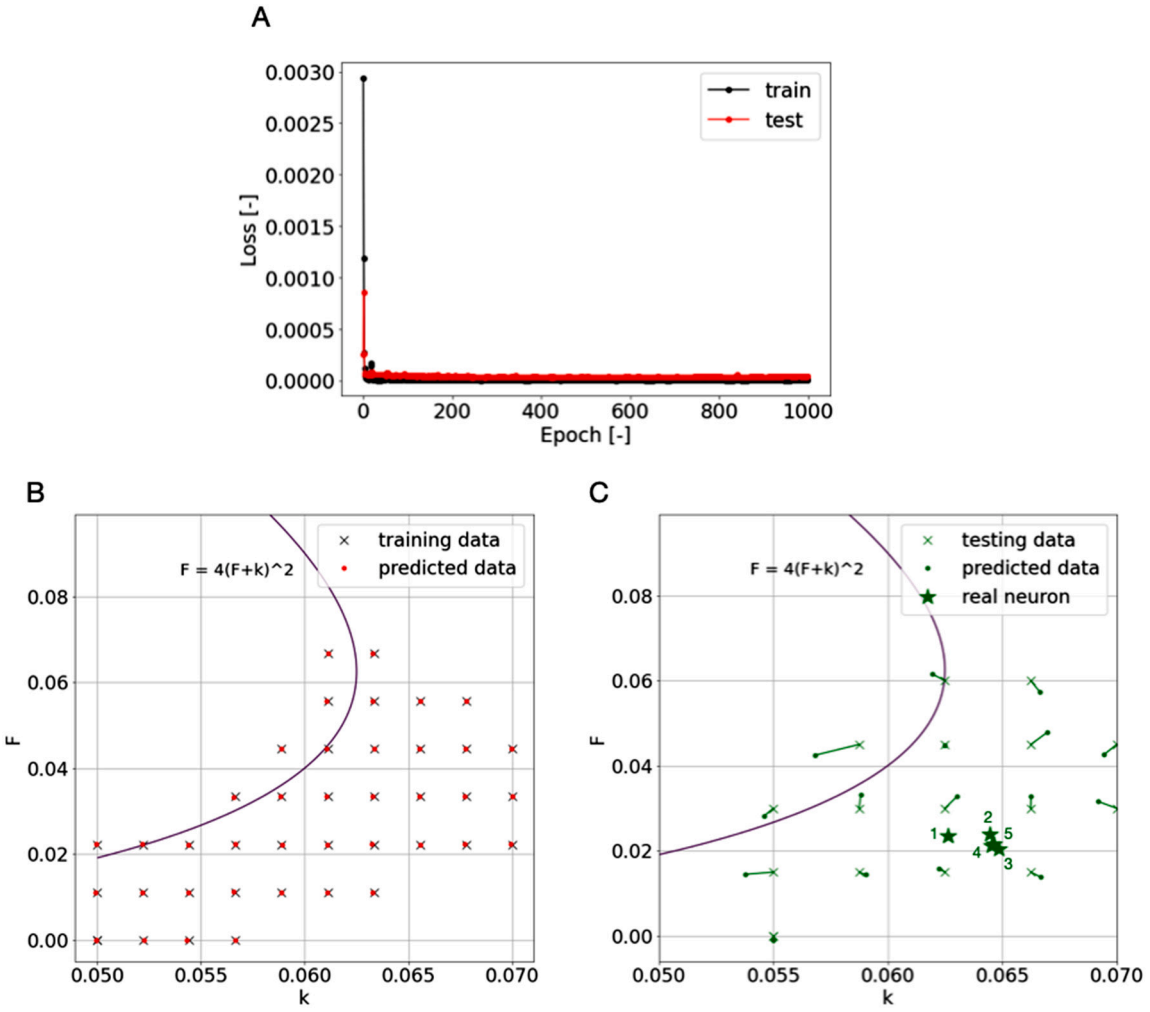

Fig. 11. Results of inverse dendrite pattern detection via CNN. (a) Loss/mean squared error as a function of epoch/iteration during training, (b) comparison between training data and predicted data, and (c) model's extrapolation and prediction of physical parameters from real neurons.

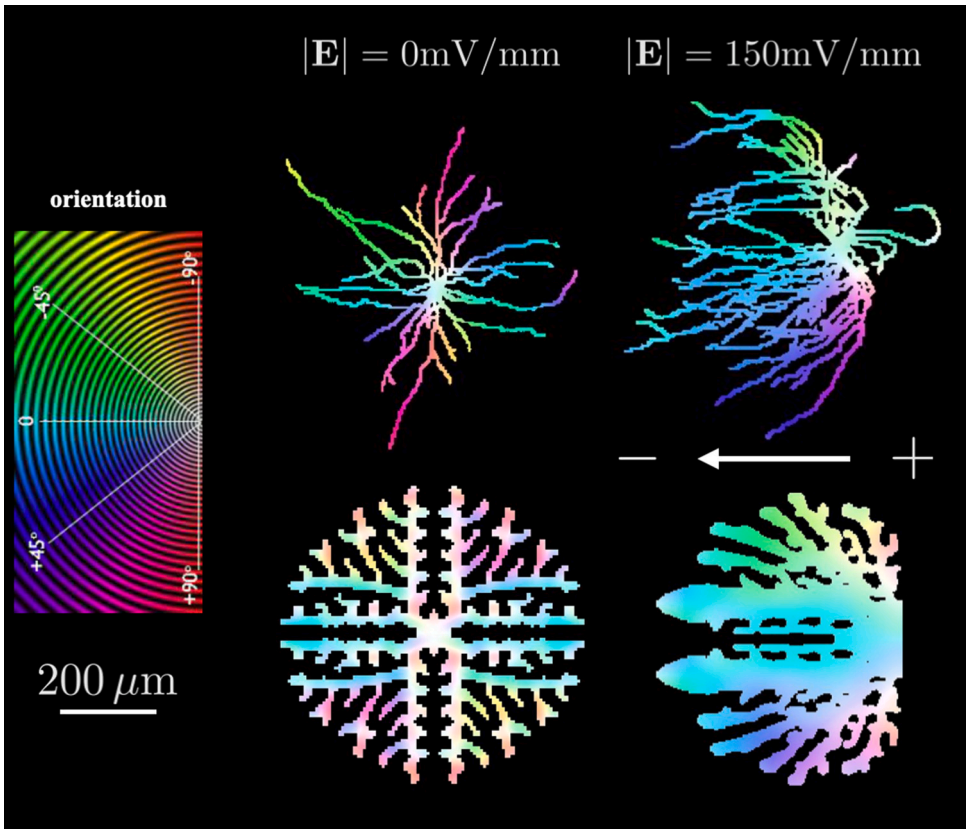

Fig. 12. Comparison between real and simulated dendrites at $\tau = 5$ h with contour plot showing orientations. without any applied electric field, the dendrites are more isotropically distributed, while a clear cathodal reorientation is observed when an electric field with a field strength of $|\mathbf{E}| = 150\,\mathrm{mV\,mm^{-1}}$ is applied horizontally. Top images are taken from [22]. (For interpretation of the references to color in this figure legend, the reader is referred to the web version of this article.)

4. Limitations and potential improvements

Our study of dendrite development is still in its infancy. Much has to be done to advance our understanding of the process and refine our mathematical formulations. First, while the Gray–Scott model produces patterns that are comparable to real dendrite morphologies, it is imperative to validate the biological mechanism our model represents through well-designed experiments. Secondly, the convolutional neural network is *not* inherently scale- and rotation-invariant. Hence, for more accurate training and extrapolation, we will need to extract scale- and rotation-independent information from dendrite patterns to use as training data. Thirdly, in this paper we focused on modeling the polarization of dendrites induced by electric fields only. However, neuronal growth is sensitive to various stimuli, including gradients of chemo-attractants, mechanical environments, and their couplings. Future multi-physics modeling endeavors should include these factors as well.

5. Concluding remarks

In this study, we have developed a dendrite growth model inspired by the activation of CaMKII via Ca^{2+} signaling. Unlike the conventional activator–inhibitor diffusion–reaction system, the model incorporates Ca^{2+} and CaMKII as a precursor and product relations. Furthermore, we incorporated electrical polarization as an advection term in our model. We implemented our model numerically using the finite-element method, which enabled us to replicate essential characteristics of dendrite growth, including self-avoidance, branching, space-filling, and electrical polarization in arbitrary geometry. Finally, we designed a convolutional neural network to inversely extract model parameters from real dendrite patterns. Overall, our work leverages modeling and simulation capabilities to unravel the possible biological mechanisms that govern the dendrite growth process.

Declaration of competing interest

The authors declare that they have no known competing financial interests or personal relationships that could have appeared to influence the work reported in this paper.

Data availability

We have shared our data and code at the online repository https://github.com/mholla/BMPHI23.

Acknowledgments

MAH acknowledges support from the National Science Foundation (CMMI 2144412). We thank Sonal Shree from Yale University for providing a clear version of the *Drosophila* larva image from her recent publication.

Appendix A. Stability analysis of Gray–Scott model

Neglecting diffusion and advection terms for a moment, the reaction terms of $g(u, v)$ and $h(u, v)$ in Eq. (2.2) allows for a trivial homogeneous steady state of

$$(u_1, v_1) = (1, 0). \tag{A.1}$$

For the following relationship between F and k to hold [57],

$$d = 1 - 4(F + k)^2/F > 0, \tag{A.2}$$

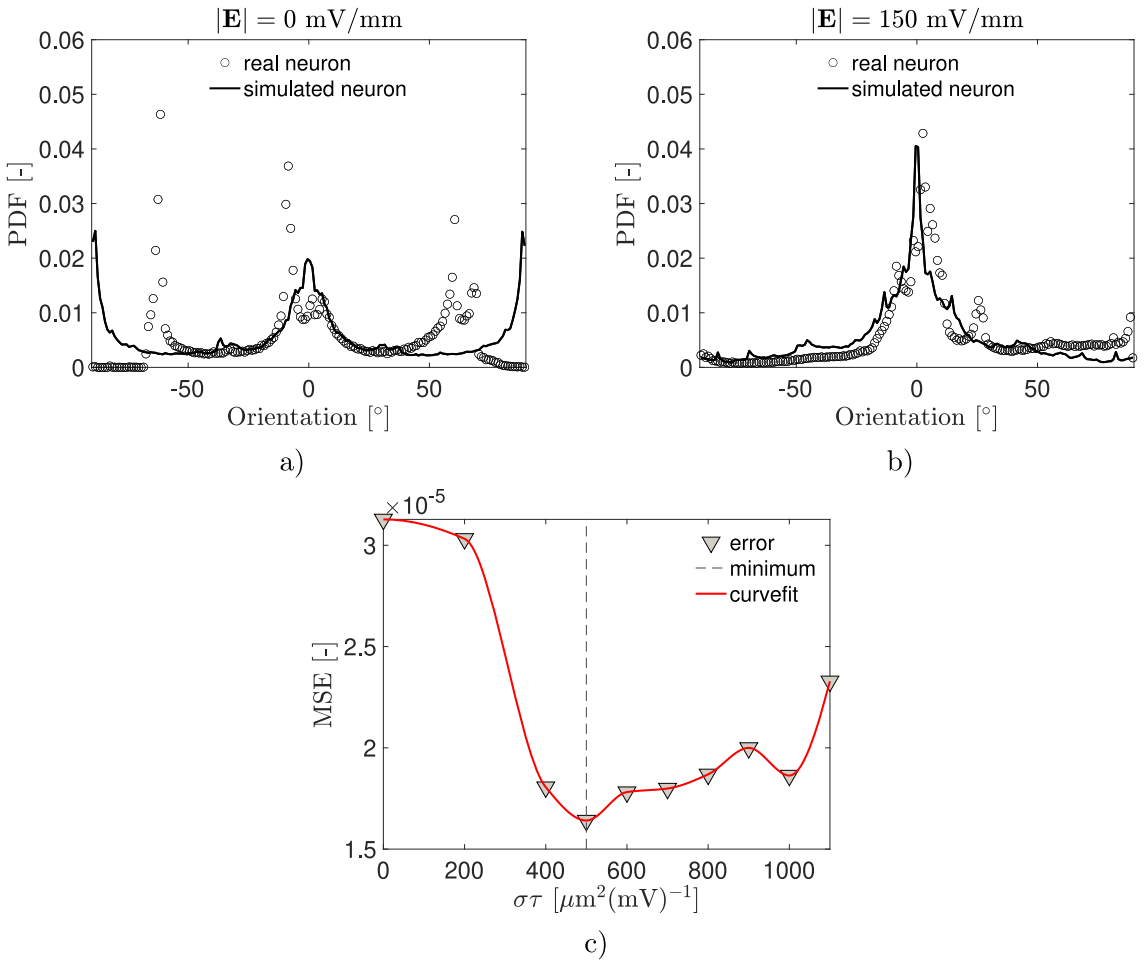

Fig. 13. Quantitative comparison between real and simulated neuron dendrites in terms of orientation distributions. (a) Controlled sample, (b) stimulated neuron, and (c) the mean squared error as a function of $\sigma\tau$. Note that gray triangles are discrete parameter trials, the solid red curve is the shape-preserving curve fit, and the dashed vertical line indicates the optimized parameter. (For interpretation of the references to color in this figure legend, the reader is referred to the web version of this article.)

the system experiences two additional steady states of

$$(u_{\mathrm{II}}, v_{\mathrm{II}}) = (\frac{1}{2}(1-\sqrt{d}), \frac{1}{2}\alpha(1+\sqrt{d})) \tag{A.3}$$

and

$$(u_{\mathrm{III}}, v_{\mathrm{III}}) = (\frac{1}{2}(1+\sqrt{d}), \frac{1}{2}\alpha(1-\sqrt{d})), \tag{A.4}$$

where the parameter $\alpha = F/(F+k)$ keeps track of the rate at which u is added in terms of the rate at which v is depleted.

To investigate the stability of all three steady states ((u_0, v_0) with the subscript 0 denotes I, II, and III), we calculate the eigenvalues of the Jacobian matrix,

$$\mathbf{J} = \begin{bmatrix} \frac{\partial g}{\partial u} & \frac{\partial g}{\partial v} \\ \frac{\partial h}{\partial u} & \frac{\partial h}{\partial v} \end{bmatrix} = \begin{bmatrix} -v_0^2 - F & -2u_0v_0 \\ v_0^2 & 2u_0v_0 - F - k \end{bmatrix}. \tag{A.5}$$

The first state $(u_{\mathrm{I}}, v_{\mathrm{I}})$, is always linearly stable, because $\mathrm{tr}(\mathbf{J}) = -2F - k < 0$ and $\det(\mathbf{J}) = F(F+k) > 0$. For the second and third state, the trace and determinant of the Jacobian are found to be $\mathrm{tr}(\mathbf{J}) = -v_0^2 + k$ and $\det(\mathbf{J}) = (F+k)(v_0^2 - F)$. In the second case, considering Eq. (A.4), $\mathrm{tr}(\mathbf{J}) > 0$ and $\det(\mathbf{J}) < 0$, indicating that it is always unstable. Finally, the third case, considering Eq. (A.3), may be stable.

We overlay the bifurcation curve $F = 4(F+k)^2$ onto the simulated morphogen u (Fig. 6). To the left of the bifurcation curve, the system experiences three steady states, and to the right of the curve, only state $(u_{\mathrm{I}}, v_{\mathrm{I}})$ exists. The saddle point of the curve locates at $(F, k) = (1/16, 1/16)$. For a more detailed study of Hopf bifurcation in the Gray–Scott model, readers can refer to [55].

Appendix B. Verification of our finite element codes

Analytically-tractable solutions for our coupled PDEs system are not trivial to obtain. As an alternative, we verify our finite element implementation by comparing independent solutions from Matlab and Abaqus.

We restrict our attention to the 1-D domain with a length of l, where the dendrite growth aligns with the applied electric field. Under the above assumption, the PDE of morphogen u in Eq. (2.5) is now given by

$$\dot{u} = D_u \frac{\partial^2 u}{\partial x^2} - uv^2 + F(1-u) \quad \text{in} \quad 0 \le x \le l. \tag{B.1}$$

Next, the PDE for morphogen v in Eq. (2.5) is now given by

$$\dot{v} - \sigma \frac{\partial \boldsymbol{\Phi}}{\partial x}\frac{\partial v}{\partial x} = D_v \frac{\partial^2 v}{\partial x^2} + uv^2 - (F+k)v \quad \text{in} \quad 0 \le x \le l. \tag{B.2}$$

Finally, the PDE for electric potential $\boldsymbol{\Phi}$ in Eq. (2.5) is now given by

$$\begin{cases} \dfrac{\partial^2 \boldsymbol{\Phi}}{\partial x^2} = 0 \quad \text{in} \quad 0 < x < l, \\ \boldsymbol{\Phi}(x=0) = \boldsymbol{\Phi}_0, \\ \boldsymbol{\Phi}(x=l) = \boldsymbol{\Phi}_l, \end{cases} \tag{B.3}$$

where $\boldsymbol{\Phi}_0$ and $\boldsymbol{\Phi}_l$ are electric potentials prescribed at the two boundary nodes. The soma initially occupies a range of $0 \le x \le (4/300)l$, inside of which we prescribe $(u, v) = (0.5, 0.25)$ and outside which we prescribe $(u, v) = (1, 0)$. Meanwhile, the electric potential is initially

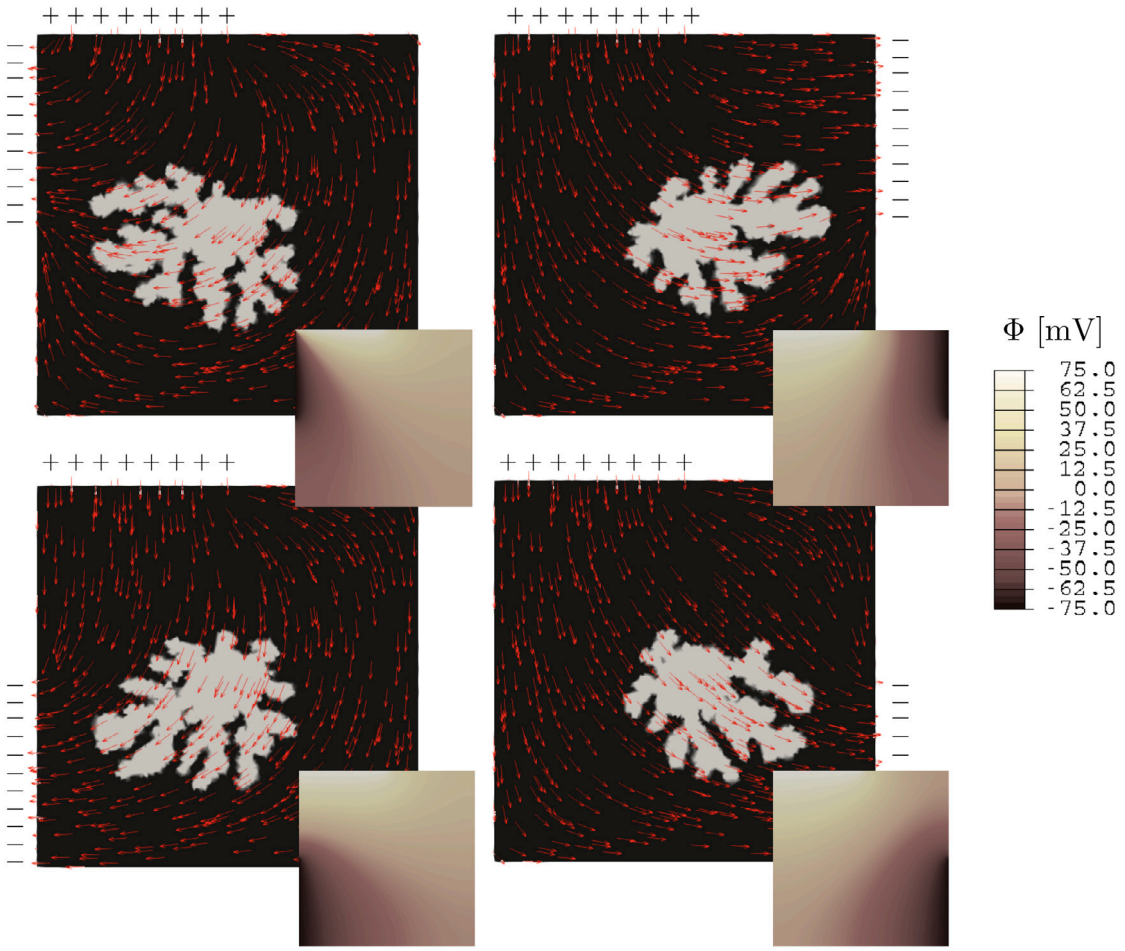

Fig. 14. 3-D simulation of dendrites growth with four different inhomogeneous electrical polarizations (viewed from the top). The red arrows indicate the direction of the electric field **E**, and the simulated contours of electric potential are shown at the corners. (For interpretation of the references to color in this figure legend, the reader is referred to the web version of this article.)

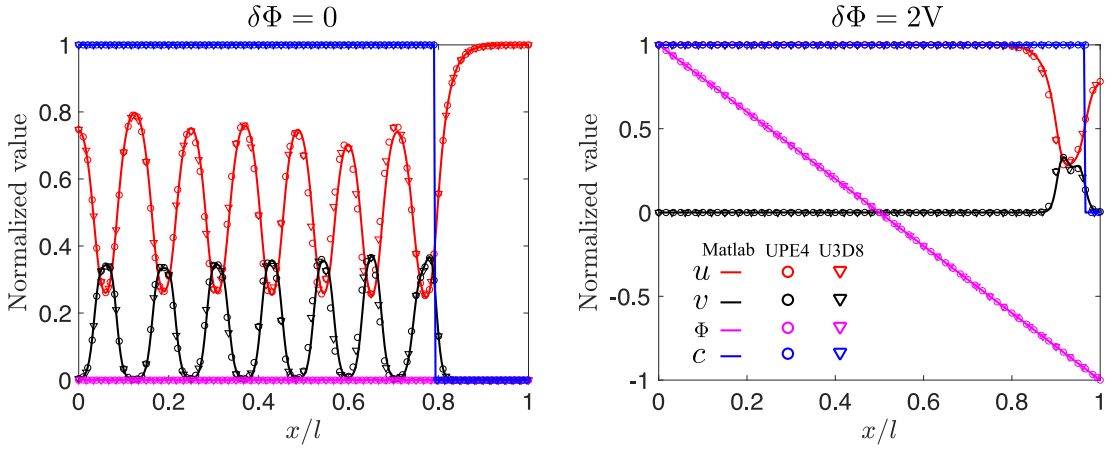

Fig. 15. Comparison of solutions using different element types of 1-D linear element in Matlab, UPE4, and U3D8 elements in Abaqus. Left: simulation with no electric potential presence. Right: simulation with an electric potential difference of $\delta\Phi = \Phi_0 - \Phi_l = 2\,\mathrm{V}$ applied across the domain. (For interpretation of the references to color in this figure legend, the reader is referred to the web version of this article.)

absent throughout the domain. The initial phase variable is $c_0 = 10^{-5}$ throughout the domain. The material parameters used for the verification are: $D_u = 0.04\,\mathrm{m^2\,s^{-1}}$, $D_v = 0.01\,\mathrm{m^2\,s^{-1}}$, $F = 0.028\,\mathrm{s^{-1}}$, $k = 0.06\,\mathrm{s^{-1}}$, $\gamma = 10\,\mathrm{s^{-1}}$, $T_r = 0.1$, and $\sigma = 0.05\,\mathrm{m^2\,s^{-1}\,V^{-1}}$. We discretize the computational domain into 300 elements and consider the two-noded linear elements in Matlab, and four-noded quadrilateral (UPE4) and eight-noded brick (U3D8) elements in Abaqus. As expected, both programs produce nearly-identical results at $t = 5000\,\mathrm{s}$, with discrepancies due to the slight differences between time-stepping algorithms, and thus we consider them fully verified (Fig. 15).

References

[1] Giorgio A. Ascoli, Duncan E. Donohue, Maryam Halavi, NeuroMorpho. Org: a central resource for neuronal morphologies, J. Neurosci. 27 (35) (2007) 9247–9251.

[2] Julie L. Lefebvre, Joshua R. Sanes, Jeremy N. Kay, Development of dendritic form and function, Annu. Rev. Cell Dev. Biol. 31 (2015) 741–777.

[3] Jürgen K. Mai, George Paxinos, The Human Nervous System, Academic Press, 2011.

[4] Winfried Denk, Kevin L. Briggman, Moritz Helmstaedter, Structural neurobiology: missing link to a mechanistic understanding of neural computation, Nat. Rev. Neurosci. 13 (5) (2012) 351–358.

[5] Margaret A. MacNeil, Richard H. Masland, Extreme diversity among amacrine cells: implications for function, Neuron 20 (5) (1998) 971–982.

[6] H. Wässle, L. Peichl, B.B. Boycott, Dendritic territories of cat retinal ganglion cells, Nature 292 (5821) (1981) 344–345.

[7] Kaoru Sugimura, Misato Yamamoto, Ryusuke Niwa, Daisuke Satoh, Satoshi Goto, Misako Taniguchi, Shigeo Hayashi, Tadashi Uemura, Distinct developmental modes and lesion-induced reactions of dendrites of two classes of Drosophila sensory neurons, J. Neurosci. 23 (9) (2003) 3752–3760.

[8] Sonal Shree, Sabyasachi Sutradhar, Olivier Trottier, Yuhai Tu, Xin Liang, Jonathon Howard, Dynamic instability of dendrite tips generates the highly branched morphologies of sensory neurons, Sci. Adv. 8 (26) (2022) eabn0080.

[9] Bartlett W. Mel, Synaptic integration in an excitable dendritic tree, J. Neurophysiol. 70 (3) (1993) 1086–1101.

[10] Zachary F. Mainen, Terrence J. Sejnowski, Influence of dendritic structure on firing pattern in model neocortical neurons, Nature 382 (6589) (1996) 363–366.

[11] Arjen Van Ooyen, Jacob Duijnhouwer, Michiel WH Remme, Jaap van Pelt, The effect of dendritic topology on firing patterns in model neurons, Network: Comput. Neural Syst. 13 (3) (2002) 311.

[12] Rachel O.L. Wong, Anirvan Ghosh, Activity-dependent regulation of dendritic growth and patterning, Nat. Rev. Neurosci. 3 (10) (2002) 803–812.

[13] Gang-Yi Wu, Hollis T. Cline, Stabilization of dendritic arbor structure in vivo by CaMKII, Science 279 (5348) (1998) 222–226.

[14] Charles C Fink, Karl-Ulrich Bayer, Jason W Myers, James E Ferrell, Howard Schulman, Tobias Meyer, Selective regulation of neurite extension and synapse formation by the β but not the α isoform of CaMKII, Neuron 39 (2) (2003) 283–297.

[15] Lori Redmond, Anirvan Ghosh, Regulation of dendritic development by calcium signaling, Cell Calcium 37 (5) (2005) 411–416.

[16] A. Kimberley McAllister, Donald C. Lo, Lawrence C. Katz, Neurotrophins regulate dendritic growth in developing visual cortex, Neuron 15 (4) (1995) 791–803.

[17] Marc Tessier-Lavigne, Corey S. Goodman, The molecular biology of axon guidance, Science 274 (5290) (1996) 1123–1133.

[18] Franck Polleux, Theresa Morrow, Anirvan Ghosh, Semaphorin 3A is a chemoattractant for cortical apical dendrites, Nature 404 (6778) (2000) 567–573.

[19] Li Yao, Abhay Pandit, Sheng Yao, Colin D. McCaig, Electric field-guided neuron migration: a novel approach in neurogenesis, Tissue Eng. B Rev. 17 (3) (2011) 143–153.

[20] Lionel F. Jaffe, Mu-Ming Poo, Neurites grow faster towards the cathode than the anode in a steady field, J. Experim. Zool. 209 (1) (1979) 115–127.

[21] Jun-Feng Feng, Jing Liu, Xiu-Zhen Zhang, Lei Zhang, Ji-Yao Jiang, Jan Nolta, Min Zhao, Guided migration of neural stem cells derived from human embryonic stem cells by an electric field, Stem Cells 30 (2) (2012) 349–355.

[22] C.D. McCaig, L. Sangster, R. Stewart, Neurotrophins enhance electric field-directed growth cone guidance and directed nerve branching, Dev. Dyn. Off. Publ. Am. Assoc. Anatom. 217 (3) (2000) 299–308.

[23] Gregor Kiddie, Douglas McLean, Arjen Van Ooyen, Bruce Graham, Biologically plausible models of neurite outgrowth, Prog. Brain Res. 147 (2005) 67–80.

[24] Bruce P. Graham, Arjen Van Ooyen, Mathematical modelling and numerical simulation of the morphological development of neurons, BMC Neurosci. 7 (1) (2006) 1–12.

[25] Hadrien Oliveri, Alain Goriely, Mathematical models of neuronal growth, Biomech. Model. Mechanobiol. 21 (1) (2022) 89–118.

[26] Giorgio A. Ascoli, Jeffrey L. Krichmar, L-Neuron: a modeling tool for the efficient generation and parsimonious description of dendritic morphology, Neurocomputing 32 (2000) 1003–1011.

[27] Sumit Nanda, Ravi Das, Shatabdi Bhattacharjee, Daniel N Cox, Giorgio A Ascoli, Morphological determinants of dendritic arborization neurons in drosophila larva, Brain Struct. Funct. 223 (3) (2018) 1107–1120.

[28] Hermann Cuntz, Friedrich Forstner, Alexander Borst, Michael Häusser, One rule to grow them all: a general theory of neuronal branching and its practical application, PLoS Comput. Biol. 6 (8) (2010) e1000877.

[29] Lothar Baltruschat, Gaia Tavosanis, Hermann Cuntz, A developmental stretch-and-fill process that optimises dendritic wiring, 2020, BioRxiv.

[30] Kaoru Sugimura, Kohei Shimono, Tadashi Uemura, Atsushi Mochizuki, Self-organizing mechanism for development of space-filling neuronal dendrites, PLoS Comput. Biol. 3 (11) (2007) e212.

[31] Kohei Shimono, Kaoru Sugimura, Mineko Kengaku, Tadashi Uemura, Atsushi Mochizuki, Computational modeling of dendritic tiling by diffusible extracellular suppressor, Genes Cells 15 (2) (2010) 137–149.

[32] Kuanren Qian, Aishwarya Pawar, Ashlee Liao, Cosmin Anitescu, Victoria Webster-Wood, Adam W Feinberg, Timon Rabczuk, Yongjie Jessica Zhang, Modeling neuron growth using isogeometric collocation based phase field method, Sci. Rep. 12 (1) (2022) 1–10.

[33] H.G.E. Hentschel, A. van Ooyen, Models of axon guidance and bundling during development, Proc. R. Soc. B 266 (1434) (1999) 2231–2238.

[34] H.G.E. Hentschel, A. Van Ooyen, Dynamic mechanisms for bundling and guidance during neural network formation, Physica A Stat. Mech. Appl. 288 (1–4) (2000) 369–379.

[35] Johannes K. Krottje, Arjen van Ooyen, A mathematical framework for modeling axon guidance, Bull. Math. Biol. 69 (2007) 3–31.

[36] Alan Roberts, Deborah Conte, Mike Hull, Robert Merrison-Hort, Abul Kalam al Azad, Edgar Buhl, Roman Borisyuk, Stephen R Soffe, Can simple rules control development of a pioneer vertebrate neuronal network generating behavior? J. Neurosci. 34 (2) (2014) 608–621.

[37] Ronen Segev, Eshel Ben-Jacob, Generic modeling of chemotactic based self-wiring of neural networks, Neural Netw. 13 (2) (2000) 185–199.

[38] Julián Andrés García-Grajales, Antoine Jérusalem, Alain Goriely, Continuum mechanical modeling of axonal growth, Comput. Methods Appl. Mech. Engrg. 314 (2017) 147–163.

[39] Hadrien Oliveri, Kristian Franze, Alain Goriely, Theory for durotactic axon guidance, Phys. Rev. Lett. 126 (11) (2021) 118101.

[40] P. Gray, S.K. Scott, Autocatalytic reactions in the isothermal, continuous stirred tank reactor: isolas and other forms of multistability, Chem. Eng. Sci. 38 (1) (1983) 29–43.

[41] Peter Gray, Stephen K. Scott, Autocatalytic reactions in the isothermal, continuous stirred tank reactor: Oscillations and instabilities in the system A+ 2B→ 3B; B→ C, Chem. Eng. Sci. 39 (6) (1984) 1087–1097.

[42] John E. Pearson, Complex patterns in a simple system, Science 261 (5118) (1993) 189–192.

[43] Roger W. Davenport, Stanley B. Kater, Local increases in intracellular calcium elicit local filopodial responses in helisoma neuronal growth cages, Neuron 9 (3) (1992) 405–416.

[44] Li Yao, Yongchao Li, The role of direct current electric field-guided stem cell migration in neural regeneration, Stem Cell Rev. Rep. 12 (3) (2016) 365–375.

[45] Anthony J. Koleske, Molecular mechanisms of dendrite stability, Nat. Rev. Neurosci. 14 (8) (2013) 536–550.

[46] Martín Abadi, Ashish Agarwal, Paul Barham, Eugene Brevdo, Zhifeng Chen, Craig Citro, Greg S. Corrado, Andy Davis, Jeffrey Dean, Matthieu Devin, Sanjay Ghemawat, Ian Goodfellow, Andrew Harp, Geoffrey Irving, Michael Isard, Yangqing Jia, Rafal Jozefowicz, Lukasz Kaiser, Manjunath Kudlur, Josh Levenberg, Dandelion Mané, Rajat Monga, Sherry Moore, Derek Murray, Chris Olah, Mike Schuster, Jonathon Shlens, Benoit Steiner, Ilya Sutskever, Kunal Talwar, Paul Tucker, Vincent Vanhoucke, Vijay Vasudevan, Fernanda Viégas, Oriol Vinyals, Pete Warden, Martin Wattenberg, Martin Wicke, Yuan Yu, Xiaoqiang Zheng, TensorFlow: Large-scale machine learning on heterogeneous systems, 2015, URL https://www.tensorflow.org/, Software available from tensorflow.org.

[47] Abaqus/Standard, Abaqus Reference Manuals, Dassault Systemes Simulia, Providence, RI, 2022.

[48] Shawn A. Chester, Claudio V. Di Leo, Lallit Anand, A finite element implementation of a coupled diffusion-deformation theory for elastomeric gels, Int. J. Solids Struct. 52 (2015) 1–18.

[49] Shuolun Wang, Martina Decker, David L Henann, Shawn A Chester, Modeling of dielectric viscoelastomers with application to electromechanical instabilities, J. Mech. Phys. Solids 95 (2016) 213–229.

[50] Craig M. Hamel, Fangda Cui, Shawn A. Chester, A finite element method for light activated shape-memory polymers, Internat. J. Numer. Methods Engrg. 111 (5) (2017) 447–473.

[51] Nikola Bosnjak, Shuolun Wang, Daehoon Han, Howon Lee, Shawn A Chester, Modeling of fiber-reinforced polymeric gels, Mech. Res. Commun. 96 (2019) 7–18.

[52] Shuolun Wang, Kengo Saito, Hiroshi Kawasaki, Maria A Holland, Orchestrated neuronal migration and cortical folding: A computational and experimental study, PLoS Comput. Biol. 18 (6) (2022) e1010190.

[53] Yann LeCun, Yoshua Bengio, et al., Convolutional networks for images, speech, and time series, in: The Handbook of Brain Theory and Neural Networks, vol. 3361, no. 10, Cambridge, MA USA, 1995, p. 1995.

[54] Kang Shen, Mary N Teruel, Kala Subramanian, Tobias Meyer, CaMKIIβ functions as an F-actin targeting module that localizes CaMKIIα/β heterooligomers to dendritic spines, Neuron 21 (3) (1998) 593–606.

[55] W Mazin, KE Rasmussen, Erik Mosekilde, Pierre Borckmans, Guy Dewel, Pattern formation in the bistable Gray-Scott model, Math. Comput. Simulation 40 (3–4) (1996) 371–396.

[56] Fabio Giampaolo, Mariapia De Rosa, Pian Qi, Stefano Izzo, Salvatore Cuomo, Physics-informed neural networks approach for 1D and 2D Gray–Scott systems, Adv. Model. Simul. Eng. Sci. 9 (1) (2022) 1–17.

[57] Alan Mathison Turing, The chemical basis of morphogenesis, Bull. Math. Biol. 52 (1) (1990) 153–197.

[58] Benoit Ladoux, René-Marc Mège, Xavier Trepat, Front–rear polarization by mechanical cues: From single cells to tissues, Trends Cell Biol. 26 (6) (2016) 420–433.